Linear Disturbance Amplification Over Blunted Flat Plates in High-Speed Flows

Anton Scholten,[*]

North Carolina State University, Raleigh, NC 27695, USA

Hemanth Goparaju,[†] Datta Gaitonde,[‡]

Ohio State University, Columbus, OH 43210, USA

Pedro Paredes,[§]

National Institute of Aerospace, Hampton, VA 23666, USA

Meelan M. Choudhari, [¶] Fei Li, [‖]

NASA Langley Research Center, Hampton, VA 23681, USA

Modal and nonmodal instability characteristics of cylindrically blunted flat plates with varying leading edge radii are described for Mach 4 and Mach 6 freestream conditions. The selection of leading edge radii and freestream parameters is informed by experimental conditions. The investigation of this 2D problem provides a slow entropy layer swallowing which allows for an isolated development of perturbations seeded upstream within different wall-normal regions of the flow. At both Mach numbers, a decrease in modal instability amplification was seen as the leading edge radius was increased. Nonmodal analysis reveals amplifying perturbations in the boundary layer as well as in the entropy layer. The medium bluntness regime exhibits the strongest amplification of nonmodal disturbances that is nonmonotonic in character. Small amplitude boundary forcing at the plate surface or volumetric forcing at various wall-normal heights was used to account for receptivity effects. While wall forcing effectively induced modal instabilities, only an actuation above the boundary layer captured disturbances that amplify within the entropy layer. The optimal nonmodal theory's entropy-layer disturbance evolution exhibited outstanding agreement with controlled forcing, including receptivity effects. The evolution of entropy-layer disturbances from the optimal nonmodal theory showed excellent agreement with the results of receptivity to controlled forcing. Therefore, the nonmodal optimal growth analysis may provide a useful as well as efficient technique to identify the complete disturbance spectrum in blunt hypersonic configurations, where both modal and nonmodal disturbances can amplify in the boundary-layer and entropy-layer regions.

Nomenclature

h_t	=	total enthalpy [kg m^2 s^2]
h_ξ	=	streamwise metric factor
h_ζ	=	spanwise metric factor
M	=	Mach number
N	=	Logarithmic amplification factor
$\hat{\mathbf{q}}$	=	vector of amplitude variables
$\check{\mathbf{q}}$	=	vector of disturbance function variables
$\bar{\mathbf{q}}$	=	vector of base flow variables

---

[*]Graduate Student, Department of Mechanical and Aerospace Engineering. AIAA Student Member

[†]Graduate Research Assistant, Department of Mechanical and Aerospace Engineering. AIAA Student Member

[‡]Glenn Chair Professor, Department of Mechanical and Aerospace Engineering. AIAA Fellow

[§]Senior Research Engineer, Computational AeroSciences Branch, NASA LaRC. AIAA Senior Member

[¶]Senior Research Scientist, Computational AeroSciences Branch. AIAA Fellow

[‖]Senior Research Scientist, Computational AeroSciences Branch.

$\tilde{\mathbf{q}}$	=	vector of perturbation variables
Re_∞	=	freestream unit Reynolds number [m^{-1}]
R_n	=	leading-edge radius [mm]
T	=	temperature [K]
T_w	=	wall temperature [K]
(u, v, w)	=	streamwise, wall-normal, and spanwise velocity components [m s^{-1}]
(x, y, z)	=	Cartesian coordinates
α	=	streamwise wavenumber [m^{-1}]
β	=	spanwise wavenumber [m^{-1}]
δ_h	=	boundary-layer thickness [mm]
κ	=	streamwise curvature [m^{-1}]
ω	=	disturbance angular frequency [s^{-1}]
ρ	=	density [kg m^{-3}]
(ξ, η, ζ)	=	streamwise, wall-normal, and spanwise coordinates
Superscripts		
$*$	=	dimensional value
Subscript		
∞	=	freestream value

I. Introduction

Due to the impact of laminar to turbulent transition on the skin friction and the surface heating on aerospace vehicles, the design of such vehicles requires an adequate understanding of the underlying mechanisms leading to transition. For hypersonic vehicles, in particular, these effects are significantly amplified, and yet, the exact cause behind a number of transition scenarios in the hypersonic speed regime remains unexplained at this point. Transition due to weak freestream disturbances can be categorized into three stages: boundary layer receptivity, linear growth and interactions of eigenmodes, and nonlinear breakdown to turbulence once critical amplitudes are achieved. Tollmien-Schlichting waves allow the excitement of shorter wavelengths in low-speed flows [1]. The wind tunnel experiments of Kendall [2] showed the second Mack mode as being the most dominant instability for hypersonic boundary-layers. Subsequent experimental and numerical studies confirmed that the modal growth of Mack-mode instabilities (second-mode waves) is most likely responsible for laminar-turbulent transition on sharp axisymmetric cones at zero degrees angle of attack [3]. Furthermore, Stetson's work [4] has demonstrated the effects of nosetip bluntness on the formation of an entropy layer that may extend well downstream of the nosetip region on axisymmetric cones. With an increasing nosetip radius, the onset of transition is moved downstream. This is supported by the increasing entropy layer having a stabilizing effect on the growth of the Mack-mode instabilities, thus delaying transition. However, experiments have demonstrated a slowdown in the downstream movement of the transition location, and an eventual reversal at nosetip radii greater than some critical value of nosetip bluntness. This reversal conflicts with the predictions of linear stability theory, which predicts that the Mack-mode growth is greatly reduced at the higher tip bluntness. The available linear stability analyses [5–8] agree that transition reversal cannot be predicted by only considering modal instability amplification, because Mack's second mode disturbances are strongly stabilized by the presence of the entropy layer, and the first mode, commonly responsible for the onset of transition at supersonic boundary-layer-edge conditions, is not destabilized. Additionally, the modal amplification of entropy-layer modes is marginal as reported by Refs. [9, 10].

Because of the failure of the modal instability theory to predict transition within the swallowing distance of the entropy layer, nonmodal growth was proposed by Paredes et al. [11] as the potential basis for a physics-based model for the experimentally observed onset of transition. Results indicate that stationary disturbances that are initiated in the vicinity of the nosetip can undergo relatively significant nonmodal amplification that increases with the nosetip bluntness. This finding may not provide a definitive link between transient growth and the onset of transition, but it is qualitatively consistent with the experimental observations that transition during the reversal regime on large bluntness configurations was highly sensitive to wall roughness, and additionally, was dominated by disturbances originating near the nosetip.

However, for moderately-large bluntness values, transition can occur significantly downstream from the nosetip, i.e., over the frustum of the cone [4]. For these moderately blunt conditions, experiments by Stetson [4] and Jewell et al. [12] indicated that uncontrolled nosetip roughness did not influence the transition onset location, suggesting that unsteady freestream disturbances may play a role in initiating frustum transition over moderately-large bluntness cones.

Computational analysis by Refs. [11, 13, 14] has shown significant nonmodal growth of both planar and oblique traveling disturbances that peak within the entropy layer and above the boundary-layer edge. The linear, nonmodal amplification of the Mack's energy norm associated with the nonstationary disturbances was lower than that for the three-dimensional stationary disturbances, but increased as the nosetip bluntness was increased [14]. Therefore, Paredes et al. [14] suggested that nonstationary nonmodal traveling disturbances that peak within the entropy layer could lead to transition onset in the absence of appreciable modal instability amplification. Furthermore, Paredes et al. [15] demonstrated that, even though the linear nonmodal disturbances are primarily concentrated outside the boundary-layer, their nonlinear interaction can generate stationary streaks that penetrate and amplify within the boundary-layer, eventually inducing the onset of transition via the breakdown of these streaks.

Transition reversal has also been experimentally reported on blunted flat plates by Lysenko [16]. The transition mechanism is somewhat different from blunted cones due to shorter entropy-layer swallowing length and azimuthal spreading, and is the focus of this work. Recent work by Goparaju et al. [17] studied the effects of leading-edge bluntness on the receptivity and stability of the boundary layer over a flat plate at zero degrees angle of attack and Mach 6 flow conditions. Direct numerical simulations (DNS) were conducted with random forcing upstream of the model. The results show a change in the induced boundary layer disturbances as the flat-plate bluntness was increased. The instability waves for the blunter models were observed near the generalized inflection point of the entropy layer above the boundary layer edge and resembled the nonmodal entropy-layer waves captured by Paredes et al. [14] for blunt cones. Additional calculations with forcing disturbances for blunt flat-plates are presented by Goparaju and Gaitonde [18] with flow conditions corresponding to the Mach 4 flow of the wind-tunnel experiments of Lysenko [16]. Again, entropy-layer disturbances were most efficiently excited when the forcing was located above the boundary-layer edge. They also employed momentum potential theory on DNS results to provide a physics-based decomposition of the flow field (acoustic, vortical, entropic components) to study modal evolution in linear and weakly nonlinear regimes.

The present paper investigates the effect of leading-edge bluntness on the modal and nonmodal instability characteristics of the boundary layer over such blunted flat plates at Mach 4 and Mach 6. The methodologies used to study the modal and nonmodal disturbances are summarized in Section II. Then, the laminar boundary-layer flow over the selected configurations and the modal instability analysis results are presented in Section III. Concluding remarks are given in Section IV.

II. Theory

In this section, we outline the methodology used for the analysis of disturbance amplification over the blunted flat plates of interest. Following the work of Refs. [11, 14], we use the harmonic linearized Navier-Stokes equations (HLNSE) and the linear parabolized stability equations (PSE) to investigate both modal and nonmodal disturbances.

A. Governing Equations for Modal and Nonmodal Disturbances

The present work is focused on the boundary layers over two dimensional blunted flat plates in a hypersonic flow. For this problem, the computational coordinates are defined as an orthogonal, body-fitted coordinate system, with (ξ, η, ζ) denoting the streamwise, wall-normal, and spanwise coordinates, respectively, and (u, v, w) representing the corresponding velocity components. Density and temperature are denoted by ρ and T. The metric factors are defined as

$$h_\xi = 1 + \kappa\eta, \tag{1}$$
$$h_\zeta = 1, \tag{2}$$

where h_ξ and h_ζ are associated with the streamwise and spanwise curvature, respectively, and κ denotes the streamwise curvature. The Cartesian coordinates are represented by (x, y, z). The vector of perturbation variables is denoted by $\tilde{\mathbf{q}}(\xi, \eta, \zeta, t) = (\tilde{\rho}, \tilde{u}, \tilde{v}, \tilde{w}, \tilde{T})^T$, and the vector of disturbance functions is $\breve{\mathbf{q}}(\xi, \eta, \zeta) = (\breve{\rho}, \breve{u}, \breve{v}, \breve{w}, \breve{T})^T$. The vector of basic state variables is $\bar{\mathbf{q}}(\xi, \eta, \zeta) = (\bar{\rho}, \bar{u}, \bar{v}, \bar{w}, \bar{T})^T$. For two-dimensional geometries, the basic state variables are independent of the spanwise coordinate and the linear perturbations can be assumed to be harmonic in time and in the spanwise direction, which lead to the following expression for the perturbations,

$$\tilde{\mathbf{q}}(\xi, \eta, \zeta, t) = \breve{\mathbf{q}}(\xi, \eta) \exp\left[\mathrm{i}\left(\beta\zeta - \omega t\right)\right] + \text{c.c.}, \tag{3}$$

where the β is the spanwise wavenumber and ω is the angular frequency. The disturbance functions $\breve{\mathbf{q}}(\xi, \eta, \zeta)$ satisfy the HLNSE [11], which linear operators depend on the basic state variables and parameters, and on the angular frequency and spanwise wavenumber of the perturbation.

The PSE approximation to the HLNSE is based on isolating the rapid phase variations in the streamwise direction via the disturbance ansatz

$$\breve{\mathbf{q}}(\xi, \eta) = \hat{\mathbf{q}}(\xi, \eta) \exp\left[i \int_{\xi_0}^{\xi} \alpha(\xi') \, d\xi'\right], \tag{4}$$

where the unknown, streamwise varying wavenumber $\alpha(\xi)$ is determined in the course of the solution by imposing an additional constraint

$$\int_{\eta} \hat{\mathbf{q}}^* \frac{\partial \hat{\mathbf{q}}}{\partial \xi} h_{\xi} h_{\zeta} \, d\eta \, d\zeta = 0. \tag{5}$$

Hence, the amplitude functions $\hat{\mathbf{q}}(\xi, \eta, \zeta) = (\hat{\rho}, \hat{u}, \hat{v}, \hat{w}, \hat{T})^T$ vary slowly in the streamwise direction in comparison with the phase term $\exp\left[i \int_{\xi_0}^{\xi} \alpha(\xi') \, d\xi'\right]$. Substituting Eq. (4) into the HLNSE and invoking scale separation between the streamwise coordinate and the other two directions to neglect the viscous terms with streamwise derivatives, the PSE are obtained.

As discussed in Ref. [11], Eq. (5) constrains the PSE disturbances to have a unique, local wavenumber at any streamwise location, and therefore, the PSE are likely to encounter difficulties when the perturbation field includes multiple disturbances with disparate variation along the streamwise direction. Optimal growth perturbations are known to include a superposition of multiple eigenmodes of the quasiparallel disturbance equations, and therefore, the HLNSE are used in the present work to study the optimal perturbations.

The onset of laminar-turbulent transition is estimated using the logarithmic amplification ratio, the so-called N-factor, relative to the lower bound location ξ_I where the disturbance first becomes unstable,

$$N_{\phi} = -\int_{\xi_I}^{\xi} \alpha_i(\xi') \, d\xi' + \ln\left[\hat{\phi}(\xi)/\hat{\phi}(\xi_I)\right], \tag{6}$$

where $\hat{\phi}$ denotes an amplitude norm of $\hat{\mathbf{q}}$, i.e., the disturbance energy norm that is defined as

$$\hat{E}(\xi) = \frac{1}{L_{\zeta}} \int_{\eta} \hat{\mathbf{q}}(\xi, \eta, \zeta)^H \mathbf{M}_E \hat{\mathbf{q}}(\xi, \eta, \zeta) \, h_{\xi} h_{\zeta} \, d\eta, \tag{7}$$

where $\mathbf{M}_E$ is the energy weight matrix and the superscript H denotes conjugate transpose. The positive-definite energy norm used here was derived by Chu [19] and used by Mack [20] and Hanifi et al. [21] for linear stability theory. This energy norm is defined as

$$\mathbf{M}_E = \text{diag}\left[\frac{\bar{T}(\xi, \eta)}{\gamma \bar{\rho}(\xi, \eta) M^2}, \bar{\rho}(\xi, \eta), \bar{\rho}(\xi, \eta), \bar{\rho}(\xi, \eta), \frac{\bar{\rho}(\xi, \eta)}{\gamma(\gamma - 1)\bar{T}(\xi, \eta) M^2}\right]. \tag{8}$$

For the nonmodal analysis, the HLNSE are solved. The optimal initial disturbance, $\tilde{\mathbf{q}}_0$, is defined as the initial (i.e., inflow) condition at ξ_0 that maximizes the objective function, J, which is defined as a measure of disturbance growth over a specified interval $[\xi_0, \xi_1]$. The definition used in the present study correspond to the outlet energy gain [22, 23] that is defined as

$$G = \frac{E(\xi_1)}{E(\xi_0)}. \tag{9}$$

The variational formulation of the problem to determine the maximum of the objective functional J leads to an optimality system [24], which is solved in an iterative manner, starting from a random solution at ξ_0 that must satisfy the boundary conditions. The HLNSE, $\mathbf{L}\tilde{\mathbf{q}} = 0$, are used to integrate $\tilde{\mathbf{q}}$ up to ξ_1, where the final optimality condition is used to obtain the initial condition for the adjoint equations integration, $\mathbf{L}^{\dagger}\tilde{\mathbf{q}}^{\dagger} = 0$.

III. Results
This section begins with the presentation of the laminar flow solution over the different leading edge bluntness flat plates at zero degrees angle of attack in a Mach 4 and 6 flow. The basic state description is followed by modal and nonmodal analysis, as well as linear forcing analysis.

A. Laminar Boundary-Layer Flow

The present Mach 4 configurations are selected to match the direct numerical simulations carried out in Ref. [18] based on experiments conducted by Lysenko [16]. The working fluid is air and effects of chemistry and molecular vibration are negligible. The leading edge is a cylinder with bluntness that varies between R_n = 0.05, 0.5, and 2.5 mm, and corresponds to small, medium, and large leading edge bluntness, respectively, based on Stetson's [4] classification. It is followed by a flat plate of length l = 400 mm. At the higher leading edge bluntness of R_n = 2.5 mm, transition reversal was experimentally reported by Lysenko [16].

The presented results were computed with a computational grid composed of 1201×401 points along the streamwise and wall-normal directions, respectively. Enough points are clustered next to the model surface to resolve the thickness of the boundary layer. The laminar flow solutions are computed by using a second-order accurate algorithm as implemented in the finite-volume compressible Navier-Stokes flow solver VULCAN-CFD* [25]. The VULCAN-CFD solution is based on the full Navier-Stokes equations and uses the solver's built-in capability to iteratively adapt the computational grid to the bow shock. Sutherland's law for air is used to calculate the dynamic viscosity as a function of temperature. Freestream conditions are given in table 1. An isothermal wall with T_w^* = 255.5 K is used. The Mach 6 conditions were defined by keeping the stagnation temperature, freestream Reynolds number and wall temperature the same as for the Mach 4 case. Thus, the Reynolds number based on leading edge bluntness is 1265, 12650, and 63250 corresponding to R_n = 0.05, 0.5, and 2.5 mm. The Mach number contours of the basic state solutions are given in Fig. 1 for all three bluntnesses and both freestream conditions. The formation of the entropy layer downstream of the curved bow shock in the vicinity of the leading edge is reflected by the region of low Mach number values that becomes thicker as the bluntness and freestream Mach number are increased. While the entropy layer thickness decreases and gets closer to the boundary layer edge in blunt cone configurations [14, 26], the entropy layer remains nearly constant to the wall for the present cases.

Table 1   Flow conditions used for the blunted flat plates with R_n = 0.05, 0.5, and 2.5 mm.

M_∞	u_∞ [m/s]	ρ_∞ [kg/m^3]	T_∞ [K]	T_0 [K]	T_{wall} [K]	$T_{\text{wall}}/T_{\text{wall,adiabatic}}$	P_0 [Pa]	Re_∞ [m^{-1}]
4	666.32	0.1770	69.05	290	255.48	0.9959	5.3268×10^5	25.3×10^6
6	715.30	0.0744	35.37	290	255.48	1.0159	1.1926×10^6	25.3×10^6

Figure 2 shows the streamwise evolution of the boundary-layer thickness and edge Mach number over the flat plate for both aforementioned conditions. The boundary-layer edge, δ_h, is defined as the wall-normal position where $h_t/h_{t,\infty} = 0.995$, with h_t denoting the total enthalpy, i.e., $h_t = h + 0.5(\bar{u}^2 + \bar{v}^2 + \bar{w}^2)$, where $h = c_p\bar{T}$ is the static enthalpy. The edge Mach number values are extracted at a wall-normal distance equal to $1.5\delta_h$ to obtain more representative values. Increasing the bluntness of the plate from R_n = 0.05 mm to R_n = 0.5 mm slightly decreases the boundary layer thickness in the vicinity of the leading edge, but increases the boundary layer thickness further downstream. The near-leading-edge effect is more pronounced when the bluntness is changed from R_n = 0.5 mm to R_n = 2.5 mm. The larger bluntness values lead to lower edge Mach number values for both freestream Mach numbers. Wall-normal profiles of Mach number and temperature taken at selected locations are shown in Figs. 3 and 4, respectively. The streamwise Mach number evolution for Mach 4, R_n = 0.5 mm from two different grids and solvers, (VULCAN (red), SAFF (black-dashed) [18, 27]) are depicted in Fig. 3. The gradients in the boundary and entropy layers matches in both approaches, confirming the accuracy of these noncanonical base flow computations. The effect of the entropy layer on the Mach number are most visible for Mach 6 at x = 0.08 m by the nonmonotonic wall-normal gradients in Mach number above the boundary layer edge. The decrease in Mach number past the maximum, which corresponds to a bluntness-dependent wall-normal location, eventually reverses and the Mach number reaches its freestream value after the shock (not shown in Figs. 3-4 as the profiles are cutoff before the shock).

B. Linear Stability Analysis

The modal and nonmodal instability analysis of the boundary-layer over the flat plates is performed via solution of the PSE and HLNSE. The PSE are used to study the modal amplification of the boundary-layer instability waves. The logarithmic amplification factor of planar and oblique waves at ξ = 0.28 is shown in Fig. 5(a,b,c) for all flat plates at Mach 4 and in Fig. 6(a,b,c) at Mach 6. For both freestream conditions and all bluntnesses, the most amplified disturbance is found for an oblique wave. These waves correspond to Mack's first mode boundary-layer instabilities

---

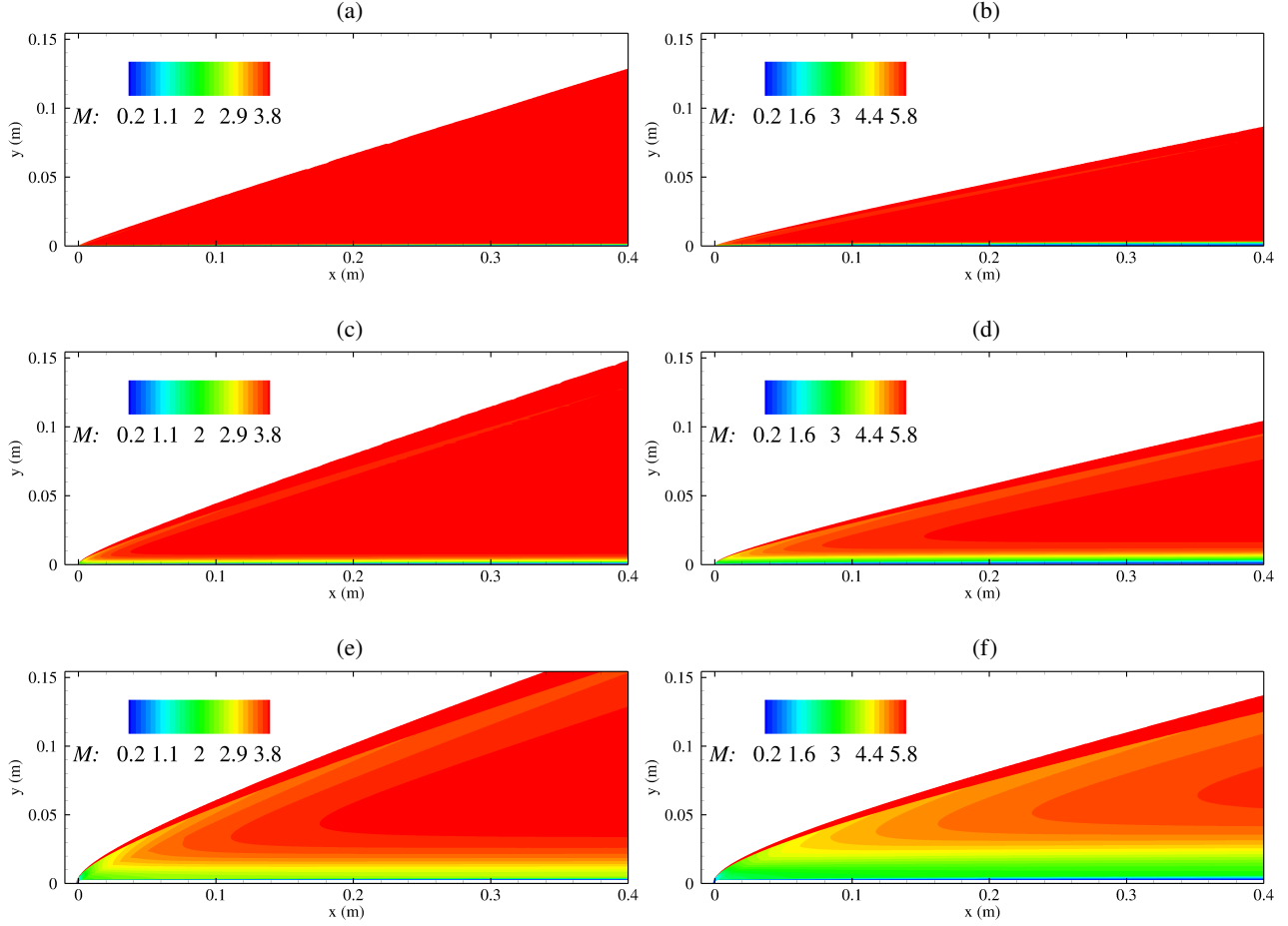*visit `http://vulcan-cfd.larc.nasa.gov` for further information about the VULCAN-CFD solver

Fig. 1 Mach contours for flat plates at (a,c,e) Mach 4 and (b,d,f) Mach 6 conditions and leading-edge bluntness of (a,b) R_n = 0.05 **mm, (c,d)** 0.5 **mm, and (e,f)** 2.5 **mm.**
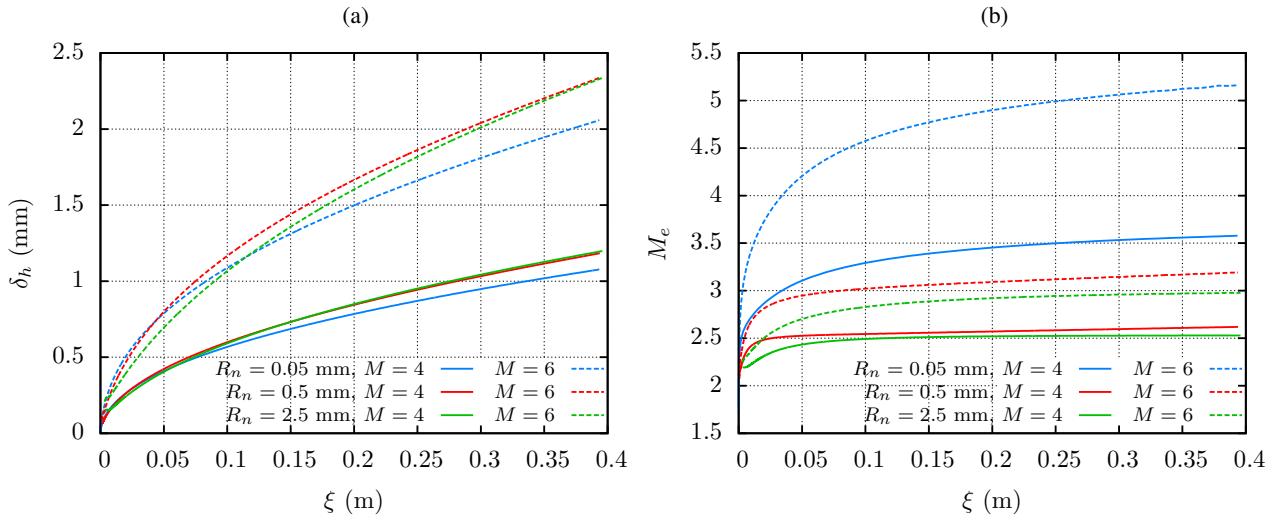

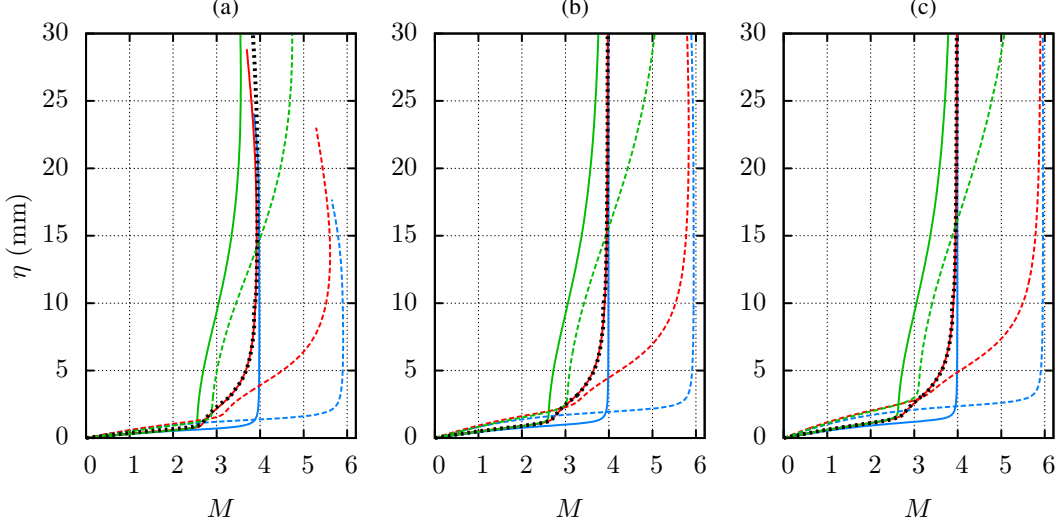**Fig. 2 Streamwise evolution of the (a) boundary-layer thickness and the (b) edge Mach number for selected bluntness parameters.**

Fig. 3 Mach number profiles for each geometry at selected streamwise locations (a) $x = 0.08$, **(b)** $x = 0.18$, **(c)** $x = 0.28$ **m. The legend remains consistent with Fig. 2. The dashed black lines are DNS results using SAFF for the Mach 4,** $R_n = 0.5$ **mm flat plate. The DNS results are reproduced from [27].**
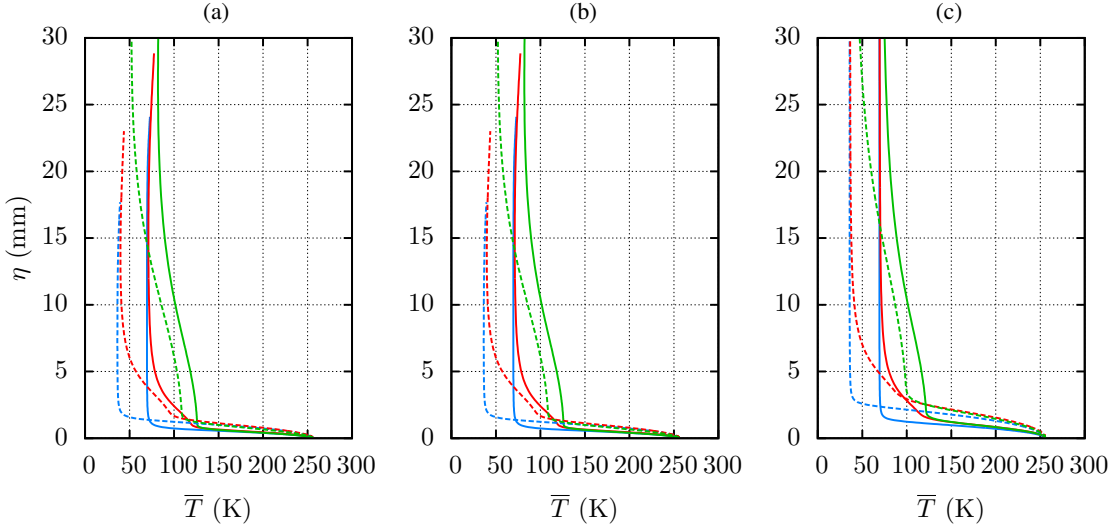
Fig. 4 Temperature profiles for each geometry at selected streamwise locations (a) $x = 0.08$, **(b)** $x = 0.18$, **(c)** $x = 0.28$ **m.**

and are also captured in the perturbation spectral signature of the forced DNS results [18]. The first mode dampens as the leading edge bluntness is increased for both freestream conditions. In addition, a planar peak is captured for the Mach 6, $R_n = 0.05$ mm geometry. Fig. 5(d,e,f) and Fig. 6(d,e,f) show the optimal disturbance energy gain based on the HLNSE for the same frequency and wavenumber space at Mach 4 and 6, respectively. Inflow and outflow locations are set to $\xi_0 = 0.02$ m and $\xi_1 = 0.28$ m. A good agreement with the most unstable mode captured by the PSE at the same streamwise location is found for each combination of leading edge radius and freestream condition. As the bluntness is increased from $R_n = 0.05$ mm to $R_n = 0.5$ mm for both Mach numbers, the frequency of the oblique wave decreases slightly. This change in frequency is a consequence of the increase in boundary-layer thickness as shown in Fig. 2(a). The wavenumber associated with the oblique wave decreases with increasing bluntness and increasing Mach number. The secondary, planar peak is identified by nonmodal analysis at higher frequencies $80 \leq f \leq 120$ kHz. The increase in

7

this planar peak with respect to R_n is nonmonotonic for both Mach numbers as it initially increases in magnitude from $R_n = 0.05$ to $R_n = 0.5$ mm but decreases from $R_n = 0.5$ to $R_n = 2.5$ mm. For Mach 6, both oblique and planar modes are comparable in amplitude at $R_n = 0.5$ mm. The forced DNS results at Mach 4 [27] also show the amplification of disturbances at the same range of frequencies between 60 and 110 kHz when the forcing is located at the entropy layer edge. The associated wavenumber and frequency for the oblique and planar disturbances are shown in table 2 as given by the optimal disturbance growth based on the HLNSE for both freestream conditions.
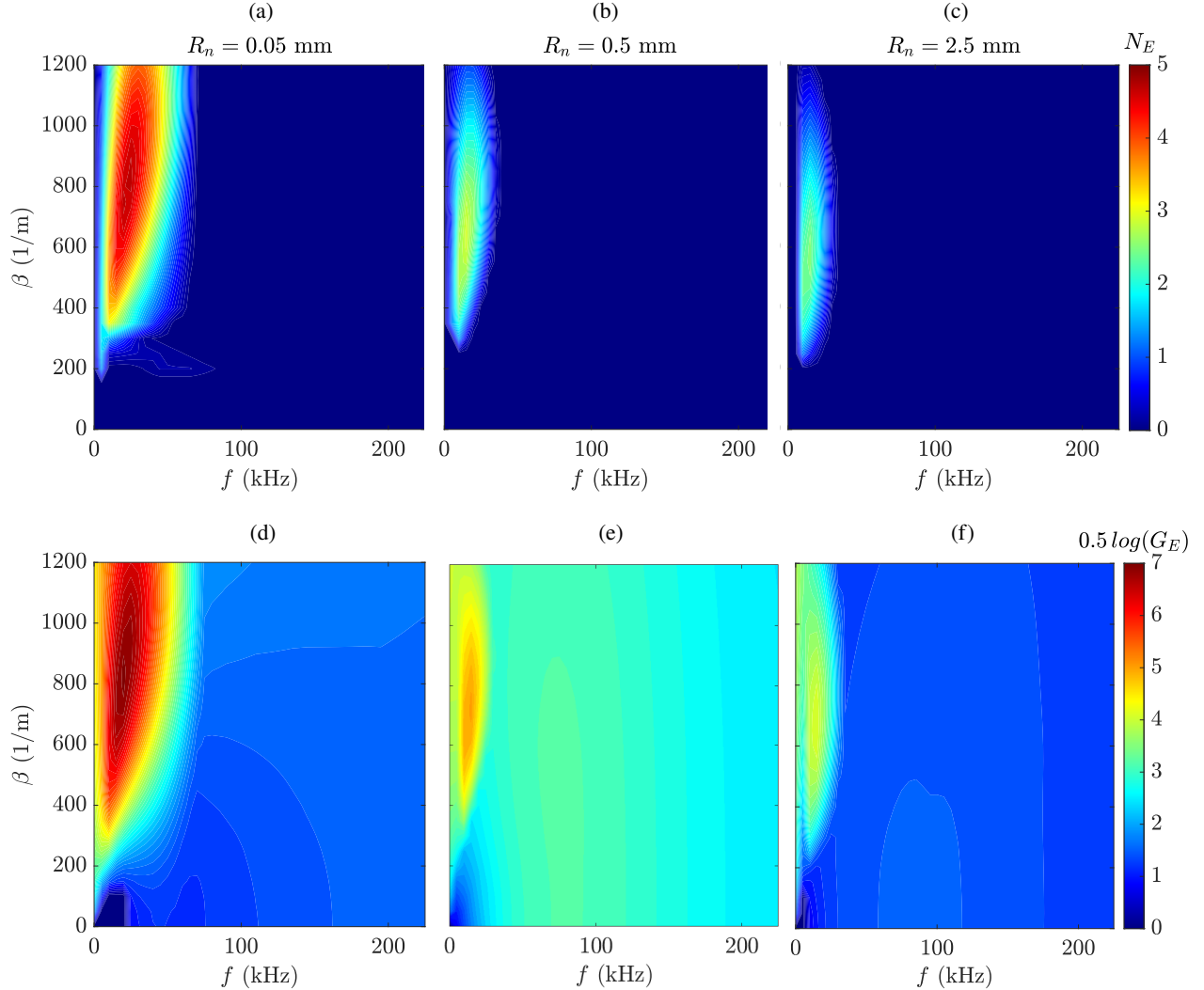
Fig. 5 N**-factor contours calculated with (a,b,c) PSE at** $\xi = 0.28$ **m and the contours of optimal disturbance energy gain over the interval** $\xi_0 = 0.02$ **m to** $\xi_1 = 0.28$ **m as calculated with (d,e,f) HLNSE for the Mach 4 flat plates with leading edge bluntness (a,d)** $R_n = 0.05$ **mm, (b,e)** $R_n = 0.5$ **mm, (c,f)** $R_n = 2.5$ **mm.**

The obtained flow perturbations for the planar disturbance at Mach 4 for the $R_n = 0.5$ mm geometry are presented in Fig. 7 and the corresponding DNS temperature perturbations are shown in Fig. 8. The DNS forcing location was set at $x = 0.06$ m and at the entropy-layer edge with a monopole width of 5 mm. The entropy-layer edge, δ_S, is defined as the location where the local entropy increment is 0.25 times the entropy increment at the wall ($\Delta S(\xi, \eta = \delta_S) = 0.25\Delta S_{wall}$) [11]. The boundary-layer and entropy-layer edges are shown as solid and dashed lines, respectively. Although the optimal planar disturbance is at $f = 80$ kHz, the DNS was performed for $f = 66.6$ kHz and thus both are set to this frequency for direct comparison. Qualitatively, the resultant mode shapes from the two approaches are equivalent, with streamwise tilted temperature fluctuations in the entropy-layer and equal streamwise wavelength. This comparison shows that the entropy-layer optimal disturbances can be realized by including receptivity effects from controlled forcing.
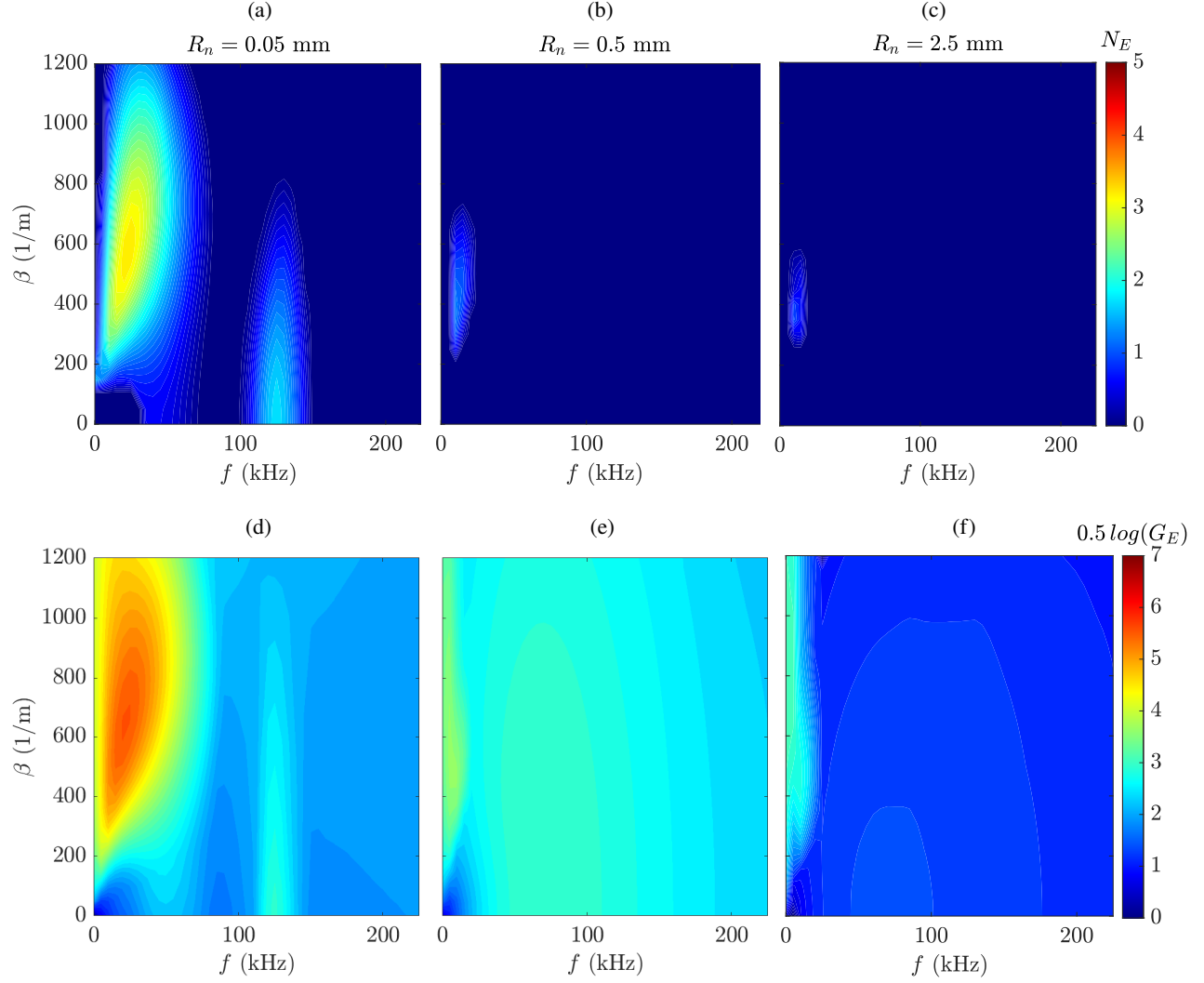
Fig. 6 N-**factor contours calculated with (a,b,c) PSE at** $\xi = 0.28$ **m and the contours of optimal disturbance energy gain over the interval** $\xi_0 = 0.02$ **m to** $\xi_1 = 0.28$ **m as calculated with (d,e,f) HLNSE for the Mach 6 flat plates with leading edge bluntness (a,d)** $R_n = 0.05$ **mm, (b,e)** $R_n = 0.5$ **mm, (c,f)** $R_n = 2.5$ **mm.**

Table 2   Frequency and spanwise wavenumber corresponding to maximum planar and oblique optimal disturbance energy gain based on the HLNSE for the different forebodies.

Leading edge radius R_n, mm	M_∞	Planar ($m = 0$) f, kHz	Oblique f, kHz	β, m^{-1}
0.05		-	20	800
0.5	4	80	15	750
2.5		80	15	650
0.05		125	20	650
0.5	6	70	10	550
2.5		65	10	450

Contours of flow perturbations associated with the maximum overall and maximum planar waves for the $R_n = 0.05$ mm flat plate at Mach 6 are shown in Figs. 9 and 10, respectively. The oblique Mack's first-mode instability with

9
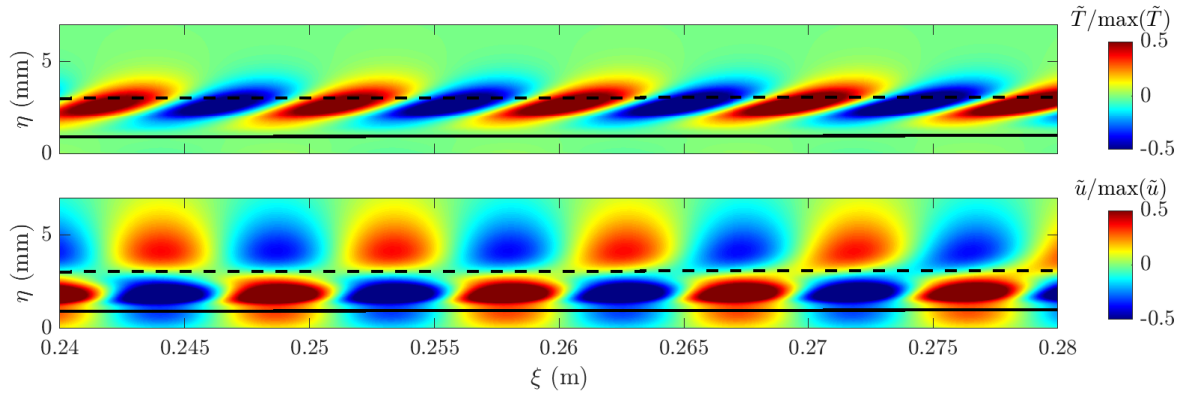
Fig. 7 Contours of flow perturbations associated with the planar disturbance with $f = 66.6$ kHz for the Mach 4, $R_n = 0.5$ mm, flat plate. The continuous black line represents the boundary-layer edge, while the dashed black line represents the entropy-layer edge.
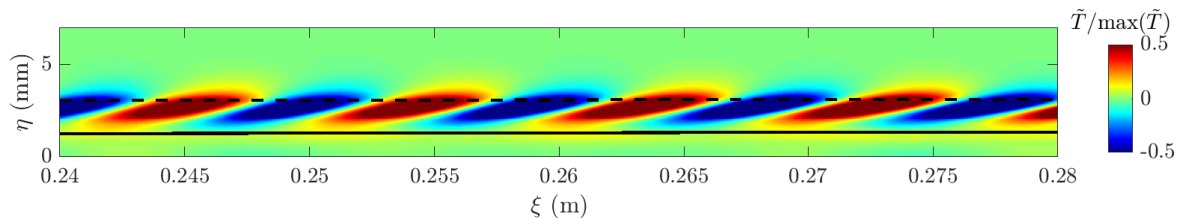

Fig. 8 DNS contours of temperature perturbations associated with the planar disturbance with $f = 66.6$ kHz for the Mach 4, $R_n = 0.5$ mm, flat plate (from Ref. [27]).

$f = 20$ kHz and $\beta = 650$ m^{-1} remains at the boundary-layer edge. In contrast, the temperature fluctuations of the planar Mack's second mode with $f = 125$ kHz are centered slightly above the boundary layer, while the streamwise velocity perturbations concentrate close to the wall.

At the higher leading edge bluntness of $R_n = 2.5$ mm, the most amplified optimal disturbance is an oblique wave with a lower frequency $f = 10$ kHz and wavenumber $\beta = 450$ m^{-1} than for $R_n = 0.05$ mm. The temperature and streamwise velocity components shown in Fig. 11 confirm this disturbance corresponds to a Mack's first mode instability. The planar optimal disturbance with $f = 65$ kHz is much further from the wall, residing between the boundary-layer and entropy-layer edges (Fig. 12). Both, the temperature and streamwise velocity perturbation components, do not penetrate the boundary-layer. The velocity component of the entropy-layer disturbance shows two layers of waves in the disturbance. A set of waves with peak fluctuations at $\eta \approx 8$ and another, with a $-180°$ phase shift, at $\eta \approx 15$ is observed. This double layer structure eventually collapses into a single wave for higher wavenumbers, visible in Fig. 13. The temperature fluctuation of this entropy-layer disturbance keeps a similar shape between $\beta = 0$ and $\beta = 450$ m^{-1}. The implications of this change in the mode shape might be significant in the transfer of energy from the entropy-layer to the boundary-layer, and will be examined in detail in future work.

C. Linear Forcing Analysis

The Mach 6 laminar basic state is forced with a disturbance given by a Gaussian bump (eq. 10) used to perturb the streamwise velocity. Flat plates with $R_n = 0.05$ and $R_n = 2.5$ mm are used and specific parameters are outlined in table 3. The streamwise forcing location is set to $\xi_0 = 0.07$ m and standard deviation $\sigma_\xi = \sigma_\eta = 0.001$ m remain constant throughout. To examine receptivity to controlled forcing, the wall-normal location is varied between being on the wall, halfway between the boundary and entropy-layer edges, and at the entropy layer edge. The forced disturbance growth is measured until $\xi_1 = 0.28$ m and compared to optimal growth analysis using the same frequency-spanwise wavenumber parametric space. For the $R_n = 0.05$ mm flat plate, the entropy layer edge is close to the boundary layer edge, i.e., the entropy layer is 51% thicker than the boundary layer, and both oblique Mack's first mode and the high frequency
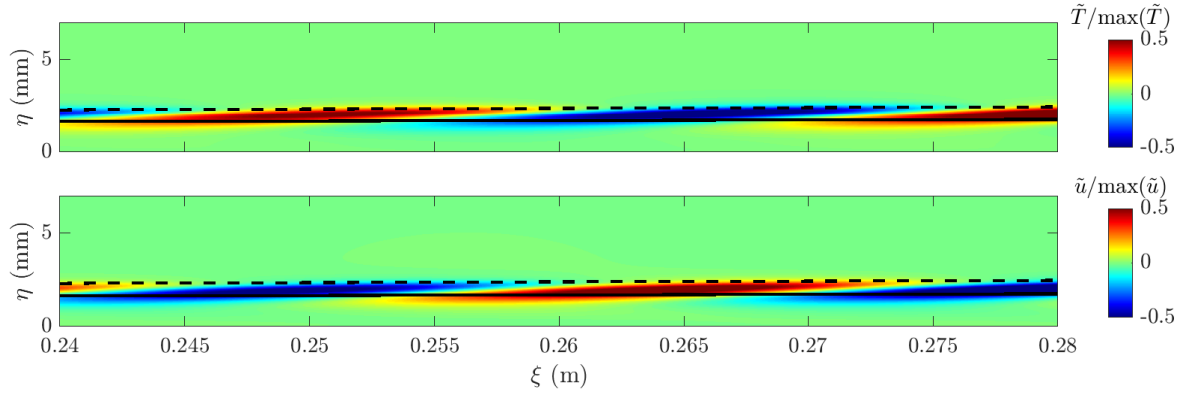
Fig. 9 Contours of flow perturbations associated with the optimal disturbance with $f = 20$ **kHz and** $\beta = 650$ **m**$^{-1}$ **for the Mach 6,** $R_n = 0.05$ **mm, flat plate. The continuous black line represents the boundary-layer edge, while the dashed black line represents the entropy-layer edge.**
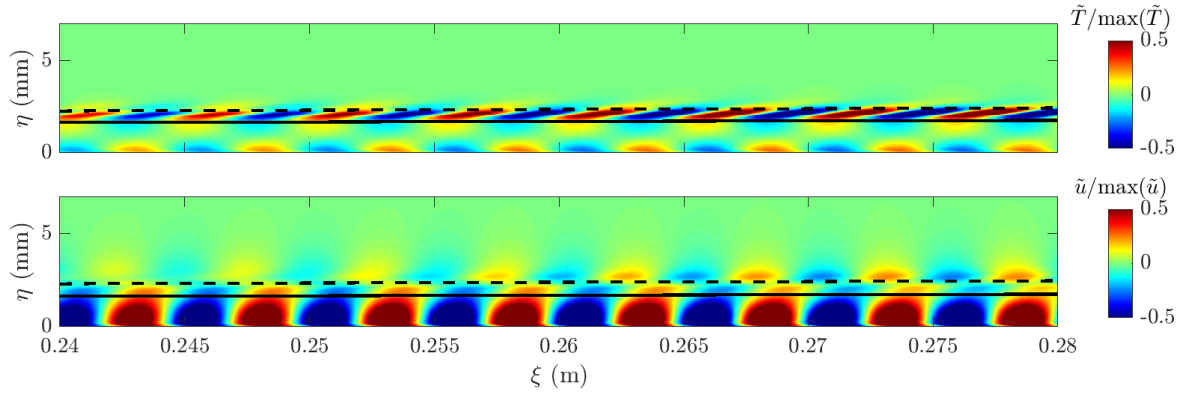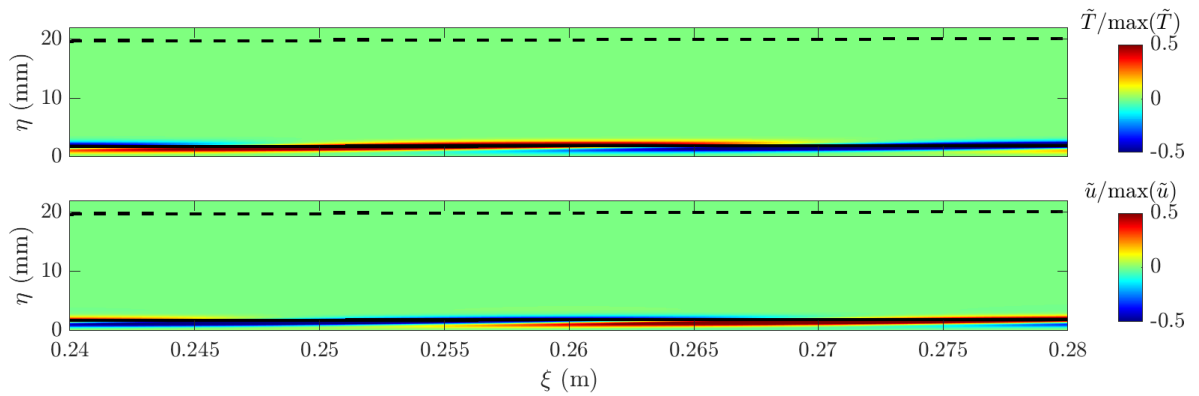

Fig. 10 Contours of flow perturbations associated with the optimal planar disturbance with $f = 125$ **kHz for the Mach 6,** $R_n = 0.05$ **mm, flat plate.**

Fig. 11 Contours of flow perturbations associated with the optimal disturbance with $f = 10$ **kHz and** $\beta = 450$ **m**$^{-1}$ **for the Mach 6,** $R_n = 2.5$ **mm, flat plate.**
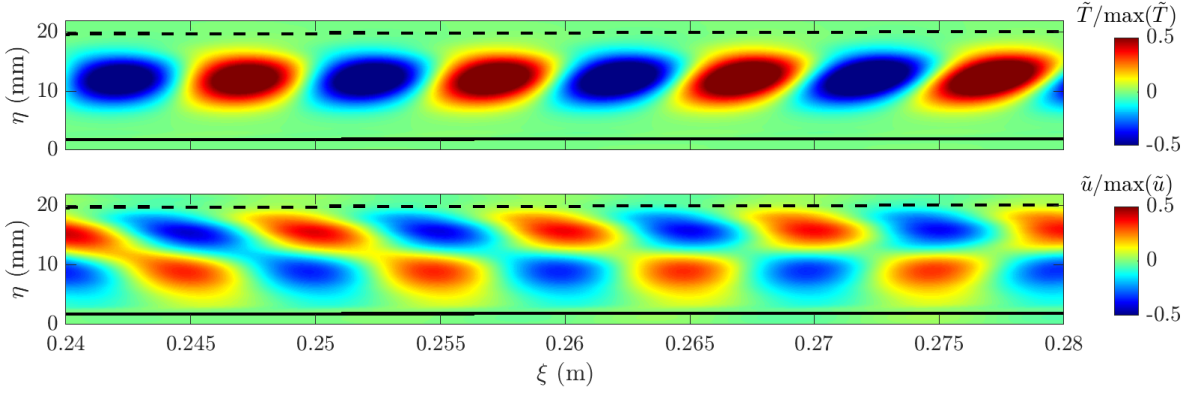
11

Fig. 12 **Contours of flow perturbations associated with the planar entropy layer disturbance with $f = 65$ kHz for the Mach 6, $R_n = 2.5$ mm, flat plate.**
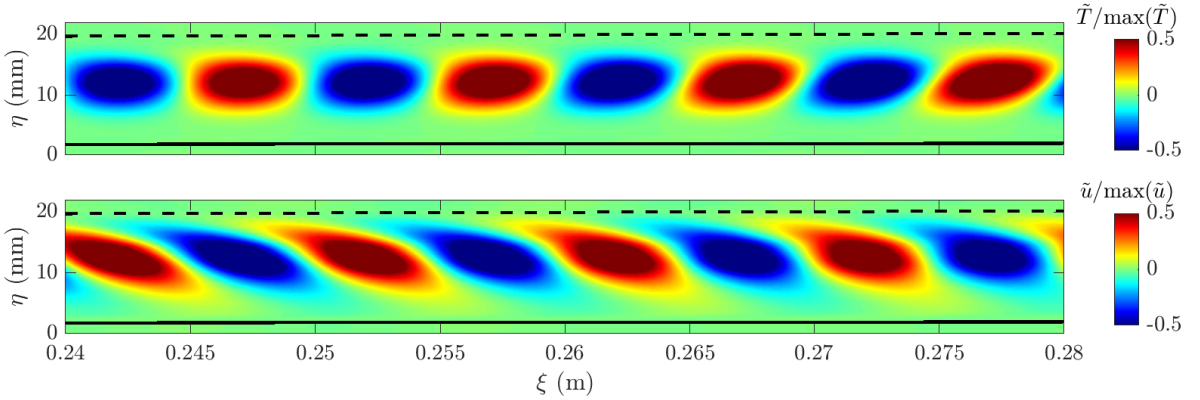

Fig. 13 **Contours of flow perturbations associated with the entropy layer disturbance with $f = 65$ kHz and $\beta = 450$ m^{-1} for the Mach 6, $R_n = 2.5$ mm, flat plate.**

$f = 120 - 125$ kHz, planar Mack's second mode disturbances are captured for all forcing locations. The results for the forcing location set at the entropy layer edge show a weaker response of the Mack's second mode disturbances and the peak switches from 125 kHz to 120 kHz. For the blunt leading edge, the oblique mode is amplified when forcing is set on the wall surface, but becomes weaker as the disturbance location is set away from the wall. The amplification of high-frequency, planar disturbances is much weaker as compared to the sharp leading edge, because the Mack's second modes become stable for the blunter cases, as shown by the modal PSE analysis results of Fig. 6(c), and is not present for surface forcing. The nonmodal entropy layer disturbances are only excited when the forcing is located above the boundary layer edge as reported by Goparaju and Gaitonde [18] who performed controlled forced DNS for the Mach 4 configurations. Hence, the nonmodal analysis provides complete spectral and modal structures about the amplifying perturbations in the boundary- and entropy-layers. By including receptivity effects, narrower bands of perturbations are amplified based on the actuator location and dynamics. The frequency and wavenumber of the different disturbance peaks are reported in table 4.

$$g(\xi, \eta) = A \exp\left(-\frac{1}{2} \left(\frac{(\xi - \xi_0)^2}{\sigma_\xi^2} + \frac{(\eta - \eta_0)^2}{\sigma_\eta^2} \right) \right) \tag{10}$$

Table 3   Forcing parameters for the sharp and blunt flat plates at Mach 6. Both geometries have an on-wall, halfway between the boundary and entropy-layer edges, and at the entropy layer edge forcing condition.

R_n, mm	δ_h, mm	δ_S, mm	ξ_0, mm	σ_ξ, mm	η_0, mm	σ_η, mm
			70	1	0	1
0.05	0.9233	1.3951	70	1	1.16	1
			70	1	1.38	1
			70	1	0	1
2.5	0.8460	15.6	70	1	8.26	1
			70	1	15.5	1

Table 4   Frequency and spanwise wavenumber corresponding to maximum planar and oblique forced disturbance energy gain based on the HLNSE at Mach 6.

Leading edge radius R_n, mm	Forcing location ξ, η	f, kHz	Planar ($m = 0$) f, kHz	Oblique β, m^{-1}
0.05		125	15	500
2.5	0.07 m, wall	-	10	450
0.05		125	20	600
2.5	0.07 m, $\frac{1}{2}(\delta_h + \delta_S)$	80	-	-
0.05		120	20	600
2.5	0.07 m, δ_S	90	-	-

IV. Summary and Concluding Remarks

For blunted flat plates at zero degrees angle of attack, laminar boundary-layer parameters as well as modal and nonmodal stability analysis results are reported. Results are presented for two different flow conditions with a constant $Re_\infty = 25.3 \times 10^6$ m^{-1} and two different Mach numbers of $M_\infty = 4$ and $M_\infty = 6$, respectively. The selected leading edge radii are 0.05, 0.5, and 2.5 millimeters, corresponding to Reynolds number values of 1265, 12650, and 63250, respectively. The Mach 4 conditions match those of previous experimental measurements [16] and DNS with external forcing [18, 27], whereas the Mach 6 conditions were selected to investigate the effect of flat plate bluntness on Mack's second mode instability. According to the modal analysis based on the parabolized stability equations, Mack's first-mode instability is the most amplified disturbance type under both flow conditions. Similarly, the most amplified disturbances identified by the nonmodal, optimal growth analysis based on the harmonic linearized Navier-Stokes equations are within the frequency and spanwise wavenumber range of Mack's first-mode instabilities. For the Mach 4 flat plates with leading-edge bluntness $R_n = 0.5$ mm and $R_n = 2.5$ mm, the optimal growth analysis also uncovers disturbances with significant amplification within a frequency range of 60 to 120 kHz, which correspond to entropy layer disturbances. At Mach 6, modal and nonmodal analysis identifies Mack's second mode instabilities over a narrow frequency range of 115 kHz to 135 kHz for $R_n = 0.05$ mm, as well as identifying a broadband, nonmodal amplification of entropy layer disturbances for the blunter flat plates with $R_n = 0.5$ mm and $R_n = 2.5$ mm. The entropy layer disturbances are amplified via nonmodal mechanisms and their peak fluctuation amplitudes occur above the boundary layer and near the outer edge of the entropy layer. Flow perturbations associated with the entropy-layer disturbances from the nonmodal results for the Mach 4, $R_n = 0.5$ mm flat plate matched well with those obtained in the previously reported forced DNS results [18]. For Mach 6 configurations with leading edge radii of 0.05 and 2.5 mm, a parametric linear force analysis is presented. When the initial disturbance is introduced near the wall, oblique first mode instabilities are generated for the sharp leading edge, yielding a higher amplification when the forced disturbance is introduced above the boundary-layer edge. For the blunt leading edge, the oblique mode is amplified for forcing at the plate surface, but remains weak when the forcing is away from the wall. Therefore, while selective, narrower bands of perturbations are captured by including receptivity to specific types of forcing, the nonmodal analysis provides more complete spectral details about the potential amplification of modal and nonmodal disturbances in the entire flow field over blunted hypersonic configurations.
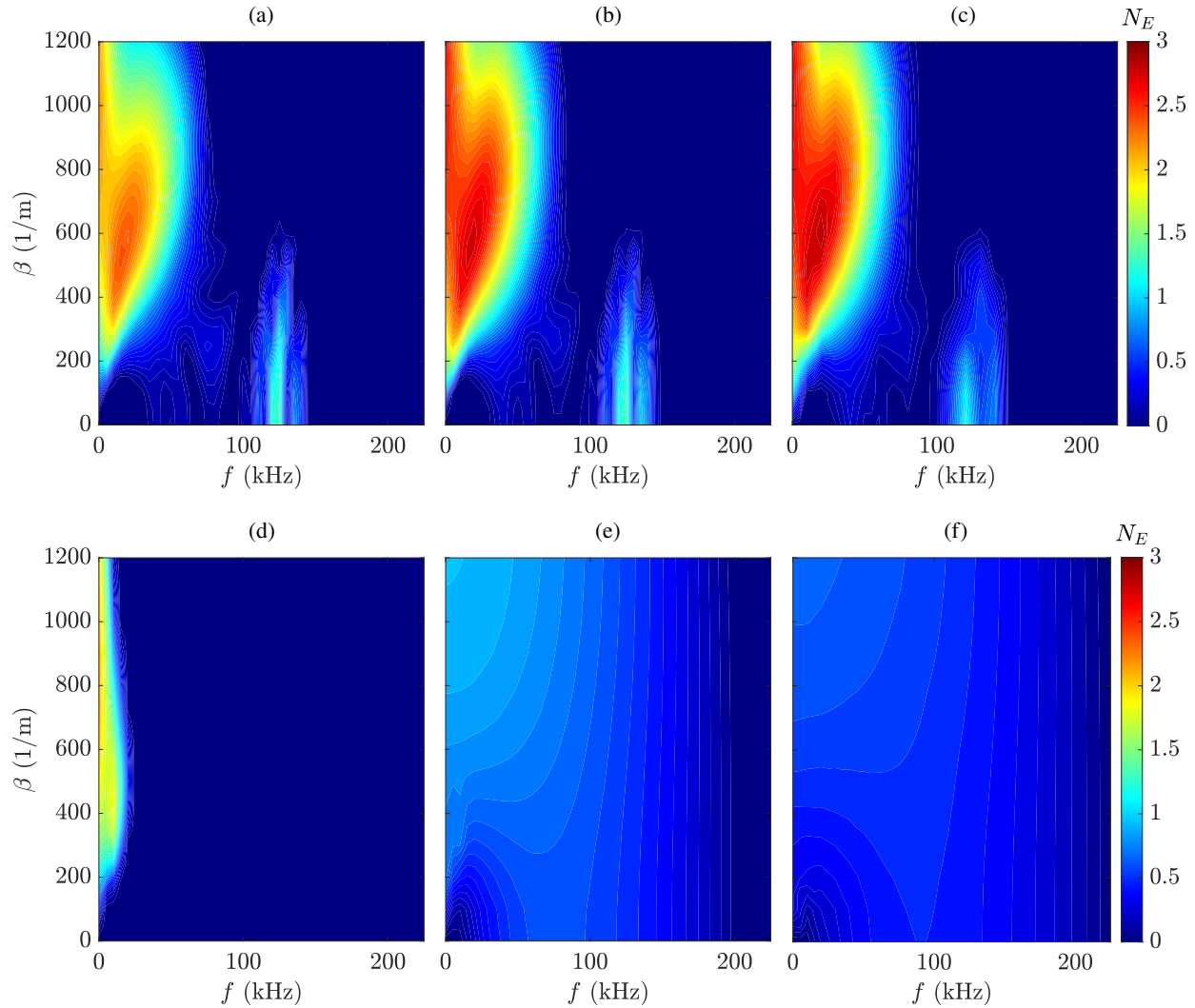
Fig. 14 **HLNSE forcing on the Mach 6 (a,b,c)** $R_n = 0.05$ **mm and (d,e,f)** $R_n = 2.5$ **mm flat plates. The forcing wall-normal location is set (a,d) at the wall, (b,e) halfway between the boundary and entropy-layer edges, and (c,f) at the entropy layer edge.**

Acknowledgments

References

[1] Saric, W., Reed, H., and Kerschen, E., "Boundary-Layer Receptivity to Freestream Disturbances," *Annual Review of Fluid Mechanics*, Vol. 34, No. 1, 2002, p. 291 (28 pages).

[2] Kendall, J., "Wind Tunnel Experiments Relating to Supersonic and Hypersonic Boundary-Layer Transition," *AIAA Journal*,

Vol. 13, No. 3, 1975, pp. 290–299. doi:10.2514/3.49694, URL https://doi.org/10.2514/3.49694.

[3] Schneider, S., "Hypersonic Laminar-Turbulent Transition on Circular Cones and Scramjet Forebodies," *Progress in Aerospace Sciences*, Vol. 40, 2004, pp. 1–50. doi:10.1016/j.paerosci.2003.11.001.

[4] Stetson, K., "Nosetip Bluntness Effects on Cone Frustum Boundary Layer Transition in Hypersonic Flow," AIAA Paper 83-1763, 1983. doi:10.2514/6.1983-1763.

[5] Malik, M., Spall, R., and Chang, C.-L., "Effect of Nose Bluntness on Boundary Layer Stability and Transition," AIAA Paper 90-0112, 1990. doi:10.2514/6.1990-112.

[6] Kufner, E., Dallmann, U., and Stilla, J., "Instability of Hypersonic Flow Past Blunt Cones - Effects of Mean Flow Variations," AIAA Paper 93-2983, 1993. doi:10.2514/6.1993-2983.

[7] Marineau, E., Moraru, C., Lewis, D., Norris, J., Lafferty, J., Wagnild, R., and Smith, J., "Mach 10 Boundary-Layer Transition Experiments on Sharp and Blunted Cones," AIAA Paper 2014-3108, 2014. doi:10.2514/6.2014-3108.

[8] Jewell, J., and Kimmel, R., "Boundary Layer Stability Analysis for Stetson's Mach 6 Blunt Cone Experiments," *Journal of Spacecraft Rockets*, Vol. 54, No. 1, 2017, pp. 258–265. doi:10.2514/1.A33619.

[9] Dietz, G., and Hein, S., "Entropy-Layer Instabilities over a Blunted Flat Plate in Supersonic Flow," *Physics of Fluids*, Vol. 11, No. 1, 1999, pp. 7–9. doi:10.1063/1.869899.

[10] Fedorov, A., and Tumin, A., "Evolution of Disturbances in Entropy Layer on Blunted Plate in Supersonic Flow," *AIAA Journal*, Vol. 42, No. 1, 2004, pp. 89–94. doi:10.2514/1.9033.

[11] Paredes, P., Choudhari, M., Li, F., Jewell, J., Kimmel, R., Marineau, E., and Grossir, G., "Nosetip Bluntness Effects on Transition at Hypersonic Speeds: Experimental and Numerical Analysis," *Journal of Spacecraft Rockets*, Vol. 56, No. 2, 2019. doi:10.2514/1.A34277.

[12] Jewell, J., Kennedy, R., Laurence, S., and Kimmel, R., "Transition on a Variable Bluntness 7-Degree Cone at High Reynolds Number," AIAA Paper 2018-1822, 2018. doi:10.2514/6.2018-1822.

[13] Cook, D., Thome, J., Brock, J., Nichols, J., and Candler, G., "Understanding Effects of Nose-Cone Bluntness on Hypersonic Boundary Layer Transition using Input-Output Analysis," AIAA Paper 2018-0378, 2018. doi:10.2514/6.2018-0378.

[14] Paredes, P., Choudhari, M., Li, F., Jewell, J., and Kimmel, R., "Nonmodal Growth of Traveling Waves on Blunt Cones at Hypersonic Speeds," *AIAA Journal*, Vol. 57, No. 11, 2019. doi:10.2514/1.J058290.

[15] Paredes, P., Choudhari, M., and Li, F., "Mechanism for Frustum Tranistion over Blunt Cones at Hypersonic Speeds," *Journal of Fluid Mechanics*, Vol. 894, 2020, p. A22. doi:10.1017/jfm.2020.261.

[16] Lysenko, V., "Influence of the Entropy Layer on the Stability of a Supersonic Shock Layer and Transition of the Laminar Boundary Layer to Turbulence," *Applied Mechanics and Technical Physics*, Vol. 31(06), 1990, p. 868 (5 pages).

[17] Goparaju, H., Unnikrishnan, S., and Gaitonde, D., "Effects of Nose Bluntness on Hypersonic Boundary-Layer Receptivity and Stability," *Journal of Spacecraft Rockets*, Vol. 58, No. 3, 2021. doi:10.2514/I.A34829.

[18] Goparaju, H., and Gaitonde, D., "Receptivity and Instability of Entropy-Layer Disturbances in Blunted Plate Transition," AIAA 2021-2877, 2021. doi:10.2514/6.2021-2877.

[19] Chu, B.-T., "On the Energy Transfer to Small Disturbances in Fluid Flow (PART I)," *Acta Mechanica*, Vol. 1, No. 3, 1956, pp. 215–234.

[20] Mack, L. M., "Boundary Layer Stability Theory," Tech. Rep. Jet Propulsion Laboratory Report 900-277, California Institute of Technology, Pasadena, CA, 1969.

[21] Hanifi, A., Schmid, P., and Henningson, D., "Transient Growth in Compressible Boundary Layer Flow," *Physics of Fluids*, Vol. 8, 1996, pp. 826–837. doi:10.1063/1.868864.

[22] Andersson, P., Berggren, M., and Henningson, D., "Optimal Disturbances and Bypass Transition in Boundary Layers," *Physics of Fluids*, Vol. 11, 1999, pp. 134–150. doi:10.1063/1.869908.

[23] Luchini, P., "Reynolds-Number-Independent Instability of the Boundary Layer over a Flat Surface: Optimal Perturbations," *J. Fluid Mech.*, Vol. 404, 2000, pp. 289–309. doi:10.1017/S0022112099007259.

[24] Paredes, P., Choudhari, M., Li, F., and Chang, C.-L., "Optimal Growth in Hypersonic Boundary Layers," *AIAA Journal*, Vol. 54, No. 10, 2016, pp. 3050–3061. doi:10.2514/1.J054912.

[25] Litton, D., Edwards, J., and White, J., "Algorithmic Enhancements to the VULCAN Navier-Stokes Solver," AIAA Paper 2003-3979, 2003. doi:10.2514/6.2003-3979.

[26] Lau, K., "Hypersonic Boundary-Layer Transition: Application to High-Speed Vehicle Design," *Journal of Spacecraft Rockets*, Vol. 45, No. 2, 2012, pp. 176–183. doi:10.2514/1.31134.

[27] Goparaju, H., and Gaitonde, D. V., "Role of Entropic-Instabilities in Laminar-Turbulent Transition on a Blunted Flat Plate," *arXiv preprint arXiv:2112.10049*, 2021.